High Dispersion of CeO$_2$ on CeO$_2$/MgO Prepared under Dry Conditions and Its Improved Redox Properties

Kenji Taira * and **Reiko Murao**

Advanced Technology Research Laboratories, Nippon Steel Corporation, 20-1 Shintomi, Futtsu 293-8511, Chiba, Japan
* Correspondence: taira.e84.kenji@jp.nipponsteel.com; Tel.: +81-70-3914-4689

Abstract: Suppressing the usage of rare-earth elements is crucial for making the catalysts sustainable. Preparing CeO$_2$ nanoparticles is a common technique to reduce CeO$_2$ consumption, but such nanoparticles are prone to sinter or react with the supports when subjected to heat treatments. This study demonstrated that stable CeO$_2$ nanoparticles were deposited on MgO by the simple impregnation method. When CeO$_2$/MgO was prepared under the dry atmosphere, the CeO$_2$ nanoparticles remained ~3 nm in diameter even after being heated at 800 °C, which is much smaller than ~5 nm of CeO$_2$/MgO prepared under ambient air. Temperature-programmed reduction, temperature-programmed oxidation, X-ray photoelectron spectroscopy, and in situ X-ray diffraction studies showed that CeO$_2$/MgO exhibited higher oxygen mobility when prepared under the dry atmosphere. Dry reforming reaction demonstrated that CeO$_2$/MgO prepared under the dry atmosphere exhibited higher activity than that prepared under ambient air and pure CeO$_2$.

Keywords: CeO$_2$; MgO; dry reforming; heterogeneous catalysis; in situ XRD

1. Introduction

CeO$_2$ has been used as catalysts and additives due to its high oxygen storage capacity and moderate basicity [1]. The inherent nature of CeO$_2$ makes it attractive for chemical reactions involving oxygen removal and addition. The transformation of renewable energy to fuel gases often employs CeO$_2$ in the process. The addition of CeO$_2$ to catalysts suppresses the carbon deposition on the catalysts during the steam-reforming reactions of CH$_4$ and tar to form syngas [2,3]. CeO$_2$ also improves the resistance of Ni catalysts against H$_2$S during methanation reaction [4] and reforming reaction [3,5] by accelerating the removal of sulfur from the surface of active species. Chemical looping reaction and thermochemical reaction also proceed over CeO$_2$ [6–9]. Despite its various applications, it is preferable to reduce the total consumption of CeO$_2$. The supply and price of CeO$_2$ are volatile. Further, the environmental load during the mining and processing of rare earth elements is higher than those of base metals [10,11]. It is desired to use less CeO$_2$ to make the catalysts, as well as the process, sustainable.

Various techniques have been employed to reduce the consumption of CeO$_2$ by controlling its size and shape [12–14]. Fine CeO$_2$ nanoparticles of high surface areas are prepared by surfactant-assisted methods [15,16]. The size of CeO$_2$ particles also influences the oxygen mobility on the CeO$_2$ surface [17,18]. The lattice constant of CeO$_2$ increases as the size of nanoparticles decreased, leading oxygen vacancies to be more stable than on the coarse CeO$_2$ particles [13,19,20]. The oxygen mobility on the CeO$_2$ surface was also influenced by the plane indices of the surface. Among the low-index surfaces, CeO$_2$(110) exhibits the highest reducibility while CeO$_2$(111) is the least reducible [21–23]. The difference was attributed to the surface energy of the surface [24,25]. CeO$_2$(111) is more stable than CeO$_2$(110) and CeO$_2$(100) because it is the non-polar, close-packed surface of CeO$_2$. Meanwhile, polar CeO$_2$(100) and less-densely packed CeO$_2$(110) surfaces underwent reconstruction of their surface, forming facets containing reduced CeO$_{2-x}$ surface [12]. Such reconstruction of the

surface leads them to be more reducible than $CeO_2(111)$. Reportedly, nanorod composed of $CeO_2(110)$ surface and cubic CeO_2 nanoparticles composed of $CeO_2(100)$ surface exhibited higher catalytic activity than conventional CeO_2 nanoparticles mostly composed of $CeO_2(111)$ surface due to higher oxygen mobility on $CeO_2(110)$ and $CeO_2(100)$ surfaces at low temperatures [21–23]. However, such self-standing CeO_2 particles sinter to ~20 m^2/g or less, corresponding to 50 nm in diameter, after calcined at high temperatures >800 °C. Both nanorods and cubic CeO_2 nanoparticles transform into conventional CeO_2 nanoparticles after being exposed to such high temperatures. Al_2O_3 supports are widely employed to improve the thermal stability of CeO_2 nanoparticles. CeO_2 nanoparticles on Al_2O_3 remain ~10 nm in diameter after the heat treatment at >800 °C under the oxidizing atmosphere [26,27]. Contrary, CeO_2 and Al_2O_3 react to form $CeAlO_3$ and other oxides under reducing conditions [28–30]. Such reactions cause structural changes in the catalysts and sintering of CeO_2 nanoparticles. High-temperature tolerant CeO_2 nanoparticles are necessary to further reduce the consumption of CeO_2 under reducing conditions.

Some studies employ MgO as a support to disperse CeO_2 nanoparticles [31–34]. The melting point of MgO is ~2850 °C, which is higher than that of Al_2O_3 supports [31]. MgO is also known for its stability under reducing conditions [35]. Further, CeO_2 nanoparticles are stabilized on MgO supports without forming any composite oxides [31–34,36]. Partial oxidation of CH_4 was demonstrated over CeO_2/MgO catalysts, suggesting their stability under the reducing conditions [34,37]. However, the average diameter of CeO_2 increased to >5 nm after the calcination at 800 °C. Techniques to stabilize finer CeO_2 nanoparticles are necessary to further reduce the consumption of CeO_2.

MgO support of large surface area would contribute to stabilized CeO_2 nanoparticles. Meanwhile, the stability of MgO depends on the atmosphere to which MgO is subjected [38–42]; relative surface energies of low-index surfaces of MgO vary depending on the humidity. Polar close-packed MgO(111) surface is stabilized by hydroxylation independent of the humidity [38]. On the contrary, non-polar MgO(100) is terminated by OH only under humid conditions since the OH-termination does not contribute to the stabilization as it is on the polar surface. Under humid conditions, therefore, OH-terminated MgO(111) is more stable than OH-terminated or pristine MgO(100). Meanwhile, pristine MgO(100) is more stable than OH-terminated MgO(111) under dry conditions [38]. Further, the sintering of MgO is accelerated in the presence of water vapor [39–42]. These reports suggest that the morphology of MgO depends on the humidity of the atmosphere under which the MgO is prepared. These studies imply that the humidity can influence the catalytic activity of the catalysts containing MgO. However, no research assessed the effect of humidity on the catalytic activity and morphology of CeO_2/MgO.

This research demonstrates that CeO_2/MgO catalysts of fine CeO_2 nanoparticles by controlling the atmosphere during the preparation. Calcination in dry air realized CeO_2 nanoparticles smaller than 3 nm in diameter even after heating at 800 °C. The prepared CeO_2/MgO catalyst outperformed pure CeO_2 for dry reforming reaction although the mass ratio of CeO_2 in CeO_2/MgO was less than 1/5 of pure CeO_2.

2. Materials and Methods

2.1. Catalyst Preparation

MgO was prepared by the thermal decomposition of Mg $(OH)_2$ (FUJIFILM Wako Pure Chemical Corporation, Osaka, Japan, 0.07 µm, >99.9%). Although the thermal decomposition of $Mg(OH)_2$ is a common technique to prepare MgO, this study employed ambient air conditions and dry air conditions to see the effect of humidity. The $Mg(OH)_2$ was dried at 110 °C for 1 h and then calcined at 800 °C for 5 h in ambient air or under a dry gas flow of 20% O_2 and N_2 balance. The samples were heated at a heating rate of 4 °C /min. The flow rate of the dry gas was fixed at 100 cm^3/min for 0.3 g of the $Mg(OH)_2$. The O_2 and N_2 were supplied from gas cylinders (Taiyo Nippon Sanso Corporation, Tokyo, Japan, O_2 > 99.99995%, N_2 > 99.99995%). MgO supports prepared in ambient air and under the dry gas flow are denoted by MgO(air) and MgO(dry), respectively. CeO_2 was

deposited on the MgO supports by impregnation. An acetone solution of $Ce(NO_3)_3 \cdot 6H_2O$ (Kanto Kagaku, >98.5%) was added dropwise to the MgO supports. The samples were dried at 60 °C with continuous stirring in ambient air. Then, the samples of MgO(air) and MgO(dry) were calcined at 800 °C for 5 h in the ambient air and under the dry gas flow, respectively. The molar ratio of CeO_2 to MgO was adjusted to 0.01/0.99 or 0.05/0.95 by changing the amount of $Ce(NO_3)_3 \cdot 6H_2O$ used for impregnation. The obtained CeO_2/MgO catalysts were denoted by 0.01- or 0.05-CeO_2/MgO(air) and 0.01- or 0.05-CeO_2/MgO(dry) corresponding to the content of CeO_2 and the atmosphere for the heat treatments. A portion of the MgO was subjected to characterizations without the deposition of CeO_2. A pure CeO_2 catalyst was also prepared via a citrate method as a reference [43]. Aquatic solutions of the $Ce(NO_3)_3 \cdot 6H_2O$ and citric acid monohydrate (Kanto Kagaku, Tokyo, Japan, >99.5%) were prepared separately and mixed into a solution. The molar ratio between $Ce(NO_3)_3 \cdot 6H_2O$ and citric acid monohydrate was kept at $\frac{1}{2}$. The pH of the solution was adjusted to ~7.0 by adding an aquatic solution of ammonia (Kanto Kagaku, Tokyo, Japan, 28.0–30.0% as NH_3) dropwise. After stirring continuously for 1 h at room temperature, the solution was dried on a rotary evaporator at 60 °C to become a viscous gel. The gel was further dried at 120 °C for 3 h and calcined at 800 °C for 5 h in ambient air. The high purity of the obtained CeO_2 was confirmed by X-ray fluorescence (Table S1 can be find in the supplementary materials). Before the reaction, the obtained powdery catalysts were pelletized by a compression molding machine and then crushed to a particle size between 500 and 750 μm by stainless steel sieves.

2.2. Catalyst Characterization

The chemical composition of the catalysts was determined by an inductively coupled plasma optical emission spectrometer (ICP-OES). 0.05 g of the sample was dissolved in a mixture of nitric acid and hydrogen peroxide. The solid residue was filtrated and melted in sodium peroxide or sodium borate. The melt was heated in hydrochloric acid to extract the elements in the sample. The obtained liquids were mixed thoroughly and adjusted to a specific volume in a volumetric flask. The prepared liquid was subjected to ICP-OES (Shimadzu, Kyoto, Japan, ICPS-8100). Specific X-ray of $\lambda = 413.765$ nm was used for Ce, and those of $\lambda = 280.270$ and 383.231 nm were used for Mg. The ICP-OES detector was calibrated using reference liquids of the elements before the measurements. The composition of each catalyst was calculated from ICP-OES results assuming both Ce and Mg exist as oxides, CeO_2 and MgO, in the catalyst.

The surface areas of the catalysts were determined using the Brunauer–Emmett–Teller (BET) method from the N_2 adsorption isotherm at the temperature of liquid nitrogen (MicrotracBEL, Osaka, Japan, BELSORP MINI X). TEM images of the catalysts were taken as bright-field images with a transmission electron microscope (Thermo Fisher Scientific, MA, USA, Tecnai G2) with an accelerating voltage of 200 kV. Each sample was mounted on a carbon grid and measured on a single-tilt holder. The average particle sizes of the CeO_2 were determined using the procedure described in the supporting information of our previous paper [44]. The projected areas of more than 100 nanoparticles on the TEM images were determined with image analysis software. Then, the sphere equivalent diameter was calculated for each particle. The arithmetic mean was calculated using an obtained frequency distribution of the diameter. The total surface area of the CeO_2 particles was also estimated for each catalyst based on the frequency distribution. The morphology of the catalysts was also observed with a scanning transmission electron microscope (STEM). STEM images of the catalysts were obtained as bright-field images with a scanning electron microscope (Hitachi, Tokyo, Japan, SU9000) with an accelerating voltage of 30 kV. Energy-dispersive X-ray spectroscopy (EDS) mapping images were taken along with STEM images with an EDS detector (Oxford Instruments, Tokyo, Japan, X-max 100LE).

The redox properties of the catalysts were assessed by temperature-programmed reduction (TPR) and temperature-programmed oxidation (TPO) studies. TPR of the samples was carried out under a flow of 5% H_2/Ar. All measurements were conducted using an

automated catalyst analyzer (MicrotracBEL, Osaka, Japan, BELCAT II) equipped with a thermal conductivity detector (TCD). For the TPR measurements, 0.05 g of the sample were placed on the bottom of a quartz tube and heated to 500 °C under an Ar flow to remove impurities. The sample was then quenched to 30 °C under a flow of Ar. TPR was conducted from 30 °C to 900 °C under a constant 30 cm^3/min flow of 5% H_2/Ar gas at a heating rate of 5 °C/min. The TPO measurements were conducted using a heating chamber (PIKE Technologies, WI, USA, DiffusIR) equipped with a quadrupole mass spectrometer (QMS) (Pfeiffer Vacuum, Aßlar, Germanny, OmniStar). CO_2 is used as an oxidant gas. For each measurement, 0.0275 g of the sample were heated in a heating chamber to 550 °C under a flow of Ar and reduced for 20 min under a constant 50 cm^3/min flow of 5% H_2/Ar gas. The sample was then cooled to 100 °C under a flow of Ar. TPO was conducted at a heating rate of 20 °C/min from 100 to 740 °C under a constant 50 cm^3/min flow of 5% CO_2/Ar gas. The outlet gas was monitored by the QMS. The QMS signals corresponding to the m/z values of 2 (H_2), 28 (CO), 40 (Ar), and 44 (CO_2) were monitored throughout the reaction. The measurement cycle was ~1.0 s at a dwelling time of 0.2 s for each m/z. The gas composition was determined using the relative intensities of the signals to that of m/z 40 (Ar). The total gas concentration was normalized to 100% for each cycle. The QMS system was calibrated before the measurements. Standard gases were used to calibrate the m/z values of 2 (H_2), 28 (CO), 40 (Ar), and 44 (CO_2). The CO concentration was calculated by subtracting the fragmentation of CO_2 and background. The fragmentation ratio of CO_2 to m/z of 44 and 28 was determined using a flow of CO_2/Ar.

The crystallographic structure of the catalysts was determined using in situ X-ray diffraction (XRD) measurements with an XRD instrument (Rigaku, Tokyo, Japn, RINT-TTR III) equipped with a Co X-ray source and an Fe filter. The scanning range was set from 2θ = 20 to 80° with a 0.02° step angle at a scanning rate of 40°/min. The X-ray tube voltage and the current were 45 kV and 200 mA, respectively. The sample catalysts were crushed into powder and mounted on an infrared heating attachment (Rigaku, Tokyo, Japan, Reactor X). The infrared heating attachment was purged by a 5% H_2/N_2 flow of 150 cm^3/min under the pressure of 0.1 Mpa. H_2 was supplied from an H_2 generator (Parker Hannifin, OH, USA, H2PEM-260) and diluted with N_2 supplied from a gas cylinder (Tokyo Koatsu, Tokyo, Japan, >99.99995%). The sample was heated up to 900 °C at a heating rate of 5 °C/min under continuous gas flow. The scanning was performed every 10 °C from 200 to 900 °C. XRD measurements were also performed under ambient air with an XRD instrument (Rigaku, Tokyo, Japan, RINT-TTR III) equipped with a Cu X-ray source and an Ni filter. The scanning range was from 2θ = 20 to 70° with a 0.02° step angle at a scanning rate of 1°/min at room temperature.

The oxidation state of Ce was measured on an X-ray photoelectron spectroscopy (XPS) analyzer (ULVAC-Phi, Kanagawa, Japan, Quantum-2000). The XPS analyzer was equipped with a monochromated Al X-ray source and a charge neutralizer. The pass energy and the recording step were controlled to 29.35 eV and 0.125 eV, respectively. The binding energy of an isolated u‴ peak of $Ce3d_{3/2}$ was adjusted to 916.70 eV to correct the peak shift derived from the charge-up of the catalysts [45,46]. C1s peak of adventitious carbon was not used for the correction due to the weak intensity of the peak and the overlap with the peaks of carbonates and Ce4s [47,48].

2.3. Dry Reforming Reaction

The obtained catalysts of particle size 500 to 750 μm were subjected to the dry reforming reaction. All the test reactions were conducted at ambient pressure for 6 h at 800 °C using a tubular flow reactor The composition of the gas was fixed to 25% CH_4, 25% CO_2, and Ar as balance at a flow rate of 100 cm^3/min. The amount of catalyst was 0.1 g for all the reactions, of which space velocity was 60,000 cm^3 hr^{-1} g-cat^{-1}. The inlet and outlet gas compositions were analyzed by a gas chromatograph (Shimadzu, Kyoto, Japan, GC-2014), employing Ar as the carrier gas. The absence of N_2 eliminated peak overlap between CO

and the balance gas, which allowed the concentration of the product gases to be estimated correctly even at low CH_4 conversions.

The CH_4 conversions were calculated using a procedure described in our previous report [49], assuming a two-step reaction shown in Equations (1) and (2). We used the reaction rates for Equations (1) and (2) as parameters to reproduce the outlet gas composition by the least-squares method. The calculated reaction rates for Equation (1) were used as the CH_4 conversion rates. All the calculations were performed ignoring the carbon deposition on the catalysts and the C_2 species in the outlet gas (<50 ppm). Therefore, the total flow of CH_4 and CO_2 in the inlet gas was equal to that of CO, CO_2, and CH_4 in the outlet gas during the calculation.

$$CH_4 + CO_2 \rightarrow 2CO + 2H_2 \tag{1}$$

$$H_2 + CO_2 \rightarrow CO + H_2O \tag{2}$$

3. Results and Discussion

3.1. Characterization of the Catalysts

The content of CeO_2 in the catalysts was calculated based on the results of ICP-OES. The obtained values were compared to the nominal values calculated from the amount of nitrates used. The nominal values and the experimental values are almost identical to each other (Table 1). This result suggests that all the catalysts were prepared at the nominal chemical composition as intended.

Table 1. Morphological properties of the prepared catalysts.

	Nominal CeO_2 Content (wt%)	CeO_2 Content (ICP-OES) * (wt%)	BET Area (m²/g)	CeO_2 Diameter (nm) **	CeO_2 Area (m₂/g) ***
MgO(air)	0	0	33.1	-	-
0.01-CeO_2/MgO(air)	4.1	4.20	30.4	5.3 ± 1.3	3.8
0.05-CeO_2/MgO(air)	18.3	18.31	27.9	6.9 ± 2.0	12.5
MgO(dry)	0	0	97.7	-	-
0.01-CeO_2/MgO(dry)	4.1	4.15	58.9	2.6 ± 1.1	6.2
0.05-CeO_2/MgO(dry)	18.3	18.33	38.5	4.5 ± 1.9	15.8
CeO_2	100.0	100.0	13.5	61.6	13.5

* Contents of CeO_2 and MgO in the catalysts were experimentally determined by ICP-OES. Sum of CeO_2 and MgO was normalized to 100%. ** Arithmetic averages were calculated from TEM measurement results. Standard deviations were described after "±" for each average diameter. The diameter of pure CeO_2 was estimated as an area-weighted average assuming the particles were spheres. *** Calculated assuming that CeO_2 particles are hemisphere attaching their flat planes on MgO.

The crystallographic structure of the prepared catalysts was assessed by XRD. No peaks other than CeO_2 and MgO were observed across all of the XRD patterns (Figure 1). The diffraction patterns of CeO_2 were weaker for CeO_2/MgO catalysts than for that of pure CeO_2 because the content of CeO_2 in CeO_2/MgO was less than 20% in the mass ratio (Table 1). Further, no clear peak shift was observed for peaks of CeO_2 and MgO, suggesting that the formation of the solid solution is small. These results are in good accordance with previous studies [31,34]. The amount of CeO_2 and MgO dissolving with each other was negligible even at 1500 °C. On the other hand, a clear difference was observed between the samples in the peak shape. The broader peaks were observed for the samples prepared in the dry atmosphere than those prepared in the ambient air, suggesting the finer MgO and CeO_2 particles of the samples prepared in the dry atmosphere.

The size of the CeO_2 nanoparticles was also compared by TEM measurement (Figure 2). Small particles stuck on the large particles were assigned as CeO_2 particles based on EDS-mapping results (Figure S1). Figure 3 shows the frequency distribution of the CeO_2 diameter. The results are summarized in Table 1. Small CeO_2 clusters (<3 nm), as well as larger nanoparticles (>3 nm), were observed in all the CeO_2/MgO catalysts as reported by Tinoco et al. [32]. The average diameter of CeO_2 increased as the content of CeO_2 in the

catalysts increased; 0.05-CeO_2/MgO(air) and 0.05-CeO_2/MgO(dry) contained larger CeO_2 nanoparticles than 0.01-CeO_2/MgO(air) and 0.01-CeO_2/MgO(dry), respectively (Table 1). Meanwhile, smaller CeO_2 nanoparticles were observed on the catalysts prepared under the dry atmosphere. The 0.01-CeO_2/MgO(dry) sample contained 2.6-nm CeO_2 on average, which is smaller than 5.3-nm CeO_2 for 0.01-CeO_2/MgO(air) (Table 1). The results of TEM were in good accordance with the results of XRD; the volume-weighted average of CeO_2 nanoparticles was comparable for both TEM and XRD results (Table S2).
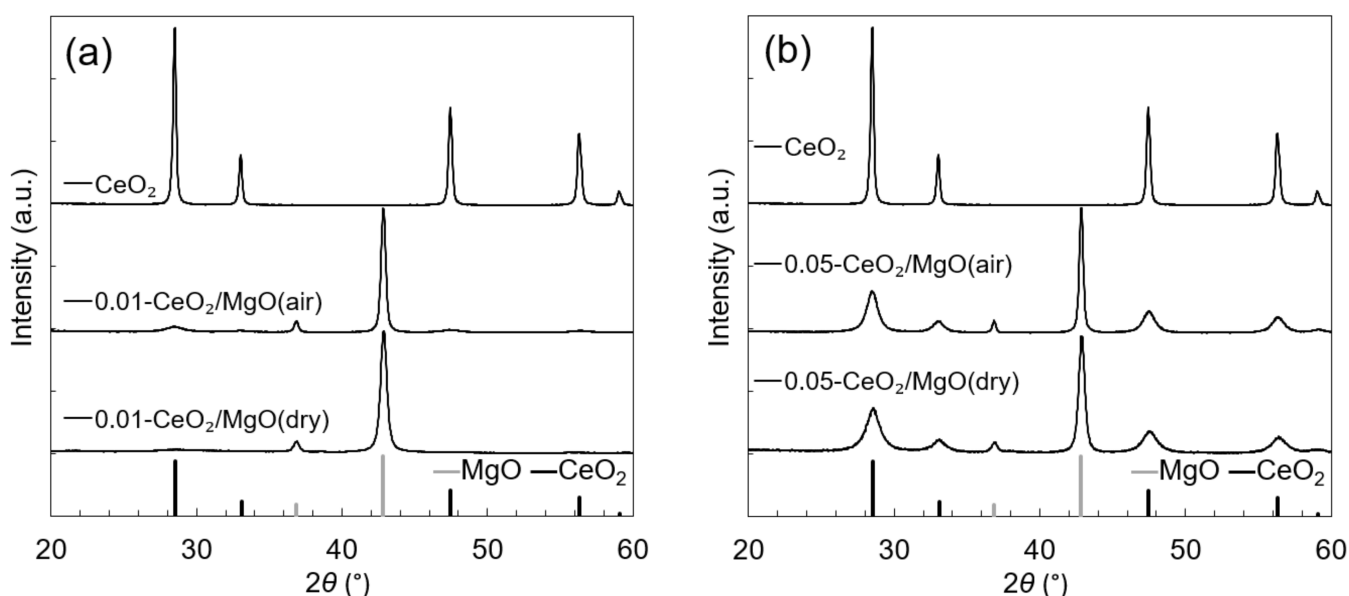
Figure 1. XRD patterns of (**a**) 0.01-CeO_2/MgO and (**b**) 0.05-CeO_2/MgO catalysts compared to that of pure CeO_2. A Cu X-ray source and an Ni filter were used. MgO and CeO_2 patterns were assigned based on the references [56,57].

The difference in the size of the CeO_2 nanoparticles was attributed to the difference in the BET area. As shown in Table 1, the BET area of MgO(dry) was approximately three times larger than that of MgO(air). MgO(dry) contained small cubic grains caused by the thermal decomposition of $Mg(OH)_2$ (Figure S2) [42]. In contrast, larger octahedral grains were observed in MgO(air) instead of in cubic grains. This difference is ascribed to the water vapor contained in the ambient air. The water vapor accelerates the sintering of MgO of <5 nm in diameter [41,42,50]. Further, the stability of each facet of MgO depends on the humidity of the atmosphere; the {100} face is favored under the dry atmosphere, but the {111} face is under the humid atmosphere [38,51]. The morphological change of MgO due to the humidity caused the sintering of CeO_2 nanoparticles during the calcination of the samples at 800 °C.

The precipitous drop in the BET surface areas of 0.01- and 0.05-CeO_2/MgO(dry) compared to MgO(dry) was attributed to the condensed nitrate solutions formed during the drying process of the impregnation. During drying, the surface of MgO is covered by $Mg(OH)_2$ since the acetone solution of $Ce(NO_3)_3$ contains water; $Ce(NO_3)_3$ $6H_2O$ was used as a precursor. Further, the acetone solution contains a small amount of water as an impurity [52]. Therefore, the equilibrium of Equation (3) is present during the drying process.

$$2Ce(NO_3)_3 + 3Mg(OH)_2 \rightleftharpoons 2Ce(OH)_3 + 3Mg(NO_3)_2 \tag{3}$$
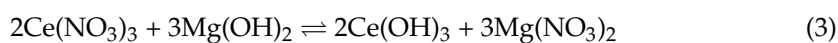
$Mg(NO_3)_2$ is soluble both in water and acetone [53,54]. Once the solution of $Mg(NO_3)_2$ formed, heterogeneous nucleation of $Mg(NO_3)_2$ and Ostwald ripening of MgO would proceed as reported for other oxides [55]. Therefore, the condensed nitrate solution would solve the MgO surface and increase its grain size, which reduced the surface area of MgO.

This result suggests that it is possible to increase the surface area by further optimizing the combination of Ce precursors and solvents.
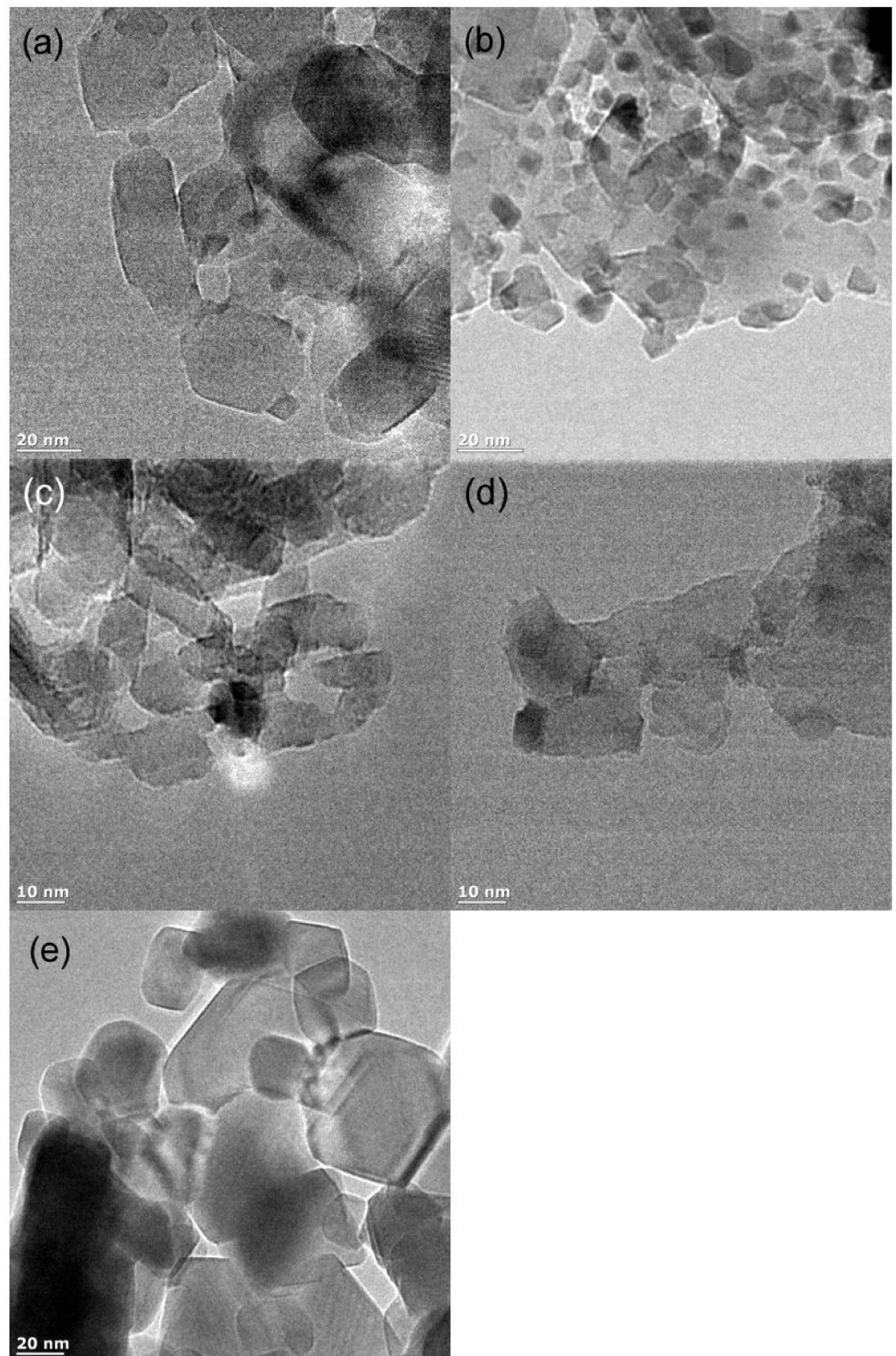

Figure 2. TEM images of (**a**) 0.01-CeO$_2$/MgO(air), (**b**) 0.05-CeO$_2$/MgO(air), (**c**) 0.01-CeO$_2$/MgO(dry), (**d**) 0.05-CeO$_2$/MgO(dry), and (**e**) CeO$_2$. STEM-EDS of the samples are shown in Figure S1.
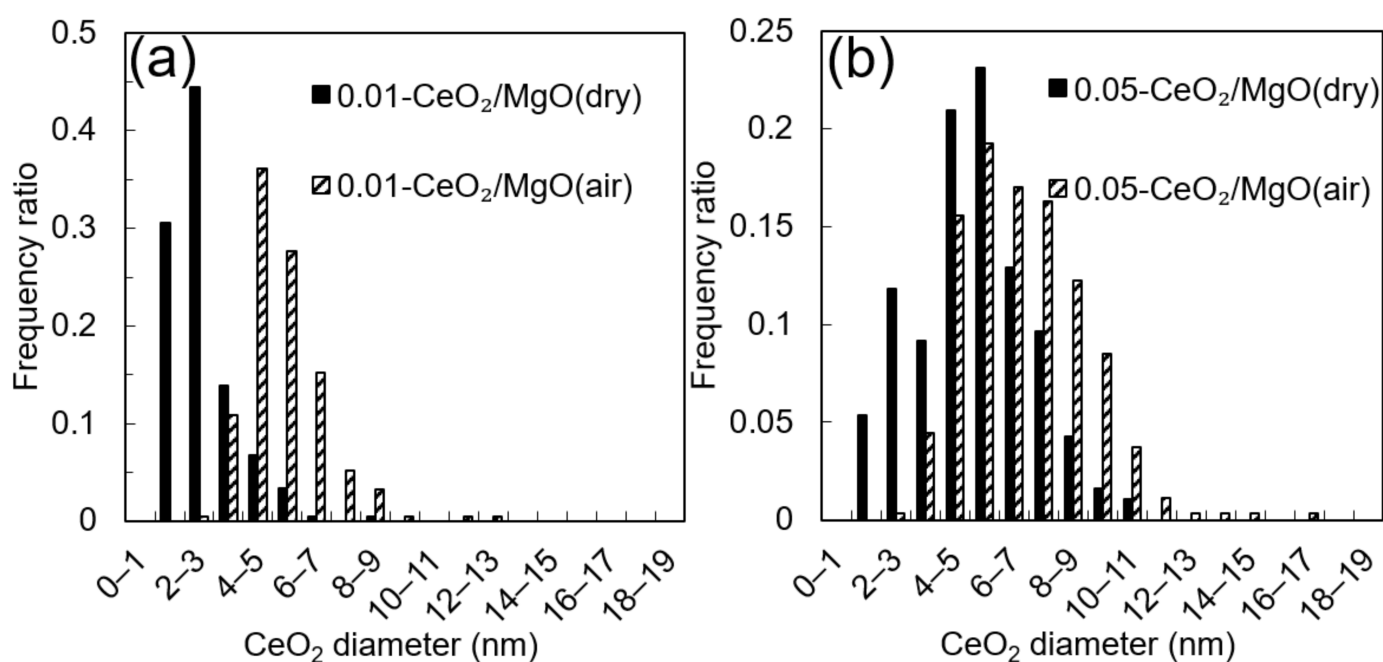
Figure 3. Frequency distribution of the CeO_2 diameter in (**a**) 0.01-CeO_2/MgO, and (**b**) 0.05-CeO_2/MgO.

3.2. Mobility of Oxygen

The mobility of oxygen species on the catalysts was assessed by the TPR measurement (Figure 4). MgO had no peaks because it is irreducible under the measurement conditions (Figure S3). All the other catalysts showed peaks at ~500 and ~800 °C, but the relative intensity of these peaks varied depending on the catalyst. The former and latter peaks are ascribed to the surface capping oxygen and the bulk lattice oxygen of CeO_2, respectively [1]. Notably, the intensity of the peaks at ~800 °C lowered as the CeO_2 content decreased while the intensity of the peaks at ~500 °C remained comparable, suggesting that the low content of CeO_2 led to finer CeO_2 nanoparticles (Figure 4a,b). This result is in good agreement with the results of the TEM measurement (Table 1, Figures 2 and 3). Further, the intensity of the peaks at ~800 °C was lower for CeO_2/MgO(dry) than for CeO_2/MgO(air) for both contents of CeO_2. These results suggest that the surface capping oxygen was predominant for the finer CeO_2 nanoparticles prepared under the dry atmosphere due to its larger surface area of CeO_2 (Table 1). In particular, 0.01-CeO_2/MgO(dry) had no peaks at ~800 °C, suggesting that both the surface capping oxygen and the lattice oxygen were removed at ~500 °C. This result is attributed to the fine CeO_2 of d = 2.6 nm in 0.01-CeO_2/MgO(dry) (Table 1). Such small CeO_2 nanoparticles have high reducibility since their unit cell expanded [13,20]. The lattice oxygen of such CeO_2 nanoparticles would diffuse ~1 nm from the center of the CeO_2 nanoparticles to the surface under the reducing atmosphere.

In addition to the intensity of the reduction peak at ~500 °C, the shape of the peak also changed depending on the preparation condition; a small shoulder appeared at ~350 °C for the samples prepared under dry conditions. This low-temperature peak was attributed to the size-dependent orientation of CeO_2 nanoparticles on the MgO surface. Reportedly, the crystallographic orientation of CeO_2 nanoparticles varies depending on the size of CeO_2; CeO_2 of 1–3 nm in diameter faces its {111} surface to the {111} surface of MgO, but CeO_2 of 10–20 nm in diameter faces its {100} surface to the {111} surface of MgO [32]. These studies suggest that preferential faceting of CeO_2 nanoparticles depends on the size of CeO_2. Further, the reducibility of the CeO_2 surface strongly depends on their faceting [23]; the reduction peak position shifted from ~500 °C for conventional CeO_2 to ~300 °C for nanorod CeO_2. Therefore, we considered that the reducibility of the surface capping oxygen was modulated by the difference in the faceting of CeO_2 nanoparticles caused by the size variation.
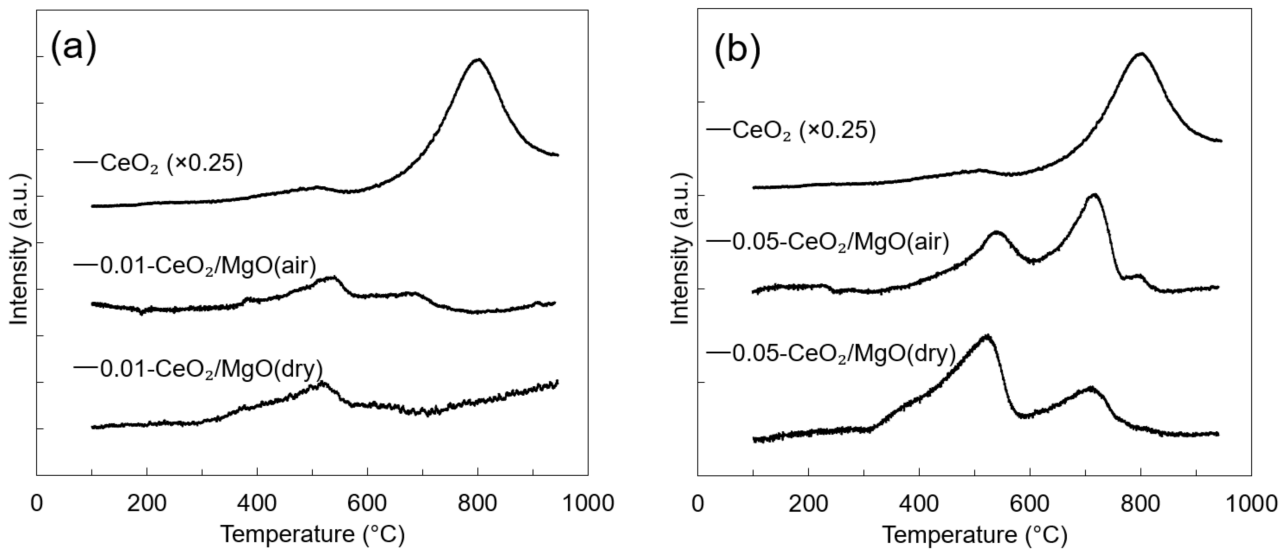
Figure 4. H_2-TPR profiles of (**a**) 0.01-CeO_2/MgO and (**b**) 0.05-CeO_2/MgO catalysts compared to that of pure CeO_2.

Redox properties of the catalysts were further assessed by TPO using CO_2 as an oxidant. The catalysts were reduced in a 5%H_2/Ar flow at 550 °C before the TPO measurements. As shown in Figure 5, the formation of CO starts at ~350 °C on all the catalysts. Further, the peak intensity is ~1.5 times higher on 0.05-CeO_2/MgO(dry) compared to those on 0.05-CeO_2/MgO(air) and pure CeO_2. These results are consistent with the H_2-TPR (Figure 4b); the reduction peak at ~500 °C on 0.05-CeO_2/MgO(dry) is larger than those of the other catalysts. CO_2 refilled the oxygen vacancies on the surface that formed during the reduction in an H_2 flow. This result also demonstrated the improved oxygen mobility of 0.05-CeO_2/MgO(dry) than those of 0.05-CeO_2/MgO(air) and pure CeO_2. Further, the results shown in Figures 4 and 5 suggest that CeO_2/MgO(dry) works as a catalyst for chemical looping combustion (CLC) [6–9]. The CLC proceeds as a two-step reaction; the catalyst is subjected to reducing conditions and then re-oxidized by CO_2 or H_2O to produce CO or H_2, which is identical to the reaction in Figure 5.
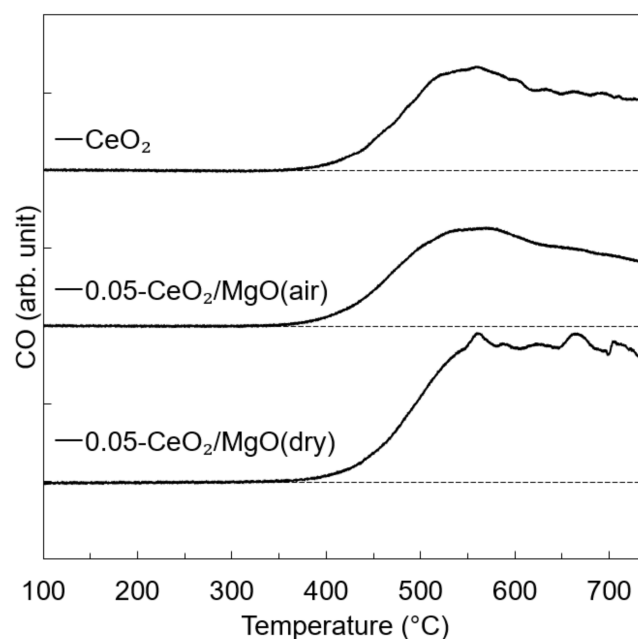

Figure 5. CO_2-TPO profiles of the reduced catalysts. The catalysts were heated at 20 °C/min in a 5% CO_2/Ar flow after the reduction at 550 °C in a 5% H_2/Ar flow.

XPS measurement was also performed on 0.01-CeO_2/MgO(air) and 0.01-CeO_2/MgO(dry) to clarify the difference of CeO_2 nanoparticles caused by the preparation condition. As shown in Figure 6, a distinct difference was observed in the spectra. There were ten peaks derived from Ce^{4+} and Ce^{3+}. The peaks annotated by v, v″, v‴, u, u″, and u‴ were attributed to Ce^{4+}. Meanwhile, v_0, v′, u_0, and u′ were due to Ce^{3+}. The binding energies of each peak are described in the caption of Figure 6. Intense peaks of Ce^{3+} denoted by v′ and u′ were observed for 0.01-CeO_2/MgO(dry). Further, the relative intensity of the $Ce3d_{3/2}$ peak denoted by u‴ was lower for 0.01-CeO_2/MgO(dry) than for 0.01-CeO_2/MgO(air), suggesting the presence of Ce^{3+} in 0.01-CeO_2/MgO(dry) [45,46]. Reportedly, the relative intensity of u‴ is not linearly correlated to the content of Ce^{3+}, but such a clear difference in the intensity of u‴ suggests that more than 30% of Ce in 0.01-CeO_2/MgO(dry) was Ce^{3+} [46,58]. This difference in the Ce^{3+} content is ascribed to the size of CeO_2. Several studies reported that CeO_2 nanoparticles smaller than 3 nm in diameter were relaxed in their crystal structure [13,19]; such small CeO_2 nanoparticles were vulnerable to in situ reductions during the exposure to X-ray under vacuum. As shown in Figure 3, 0.01-CeO_2/MgO(dry) contained a lot of CeO_2 nanoparticles smaller than 3 nm, which would be reduced during the XPS measurement. Such high reducibility of 0.01-CeO_2/MgO(dry) matched well with the results of H_2-TPR (Figure 4). 0.01-CeO_2/MgO(dry) was reduced at a lower temperature than 0.01-CeO_2/MgO(air). Here, it is noteworthy that the effect of precursors on the valence of Ce was minor because both samples were prepared using the same precursor [13].
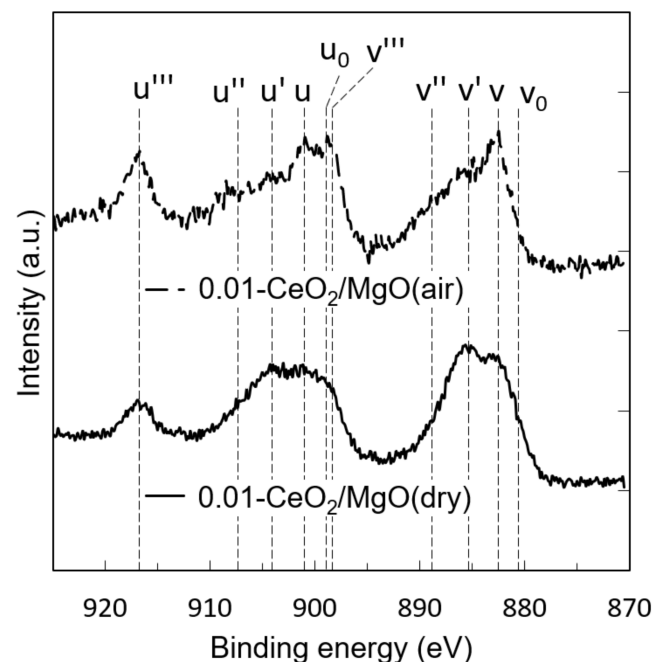

Figure 6. XPS spectra of 0.01-CeO_2/MgO(air) and 0.01-CeO_2/MgO(dry). The peak positions of v_0, v, v′, v″, v‴, u_0, u, u′, u″, and u‴ are 880.60, 882.60, 885.45, 888.85, 898.40, 898.90, 901.05, 904.05, 907.45, and 916.70 eV, respectively. The binding energies of all the peaks are identical to the values of the reference [46].

3.3. In Situ XRD Study under the Reducing Atmosphere

In situ XRD was performed to visualize the structural variation of CeO_2 nanoparticles during the reduction. Instead of 0.01-CeO_2/MgO, 0.05-CeO_2/MgO(air) and 0.05-CeO_2/MgO(dry) were used to increase the peak intensity to perform further analyses. The measurements were performed under the same condition as that of H_2-TPR, but an N_2 balance was used as a balance instead of Ar. CeO_2 was also subjected to the same measurement as a reference. The results are shown in Figure 7. Only the peaks of CeO_2 and MgO were observed in the patterns since the phase change from CeO_2 to Ce_2O_3 is

slow. The absence of Ce_2O_3 was consistent with the previous studies [1,59,60]. As shown in the patterns of CeO_2/MgO (Figure 7b,c), the peaks of MgO linearly shifted to lower 2θ as the temperature increased, suggesting a continuous thermal expansion of MgO crystals. The peaks of CeO_2 also shifted to the same direction; however, the peaks showed the inflection points at ~650 °C (Figure 7b,c). This implies that structural relaxation was caused by the removal of lattice oxygen of the CeO_2 nanoparticles. Additionally, CeO_2 in both $CeO_2/MgO(air)$ and $CeO_2/MgO(dry)$ underwent structural change at lower temperatures than pure CeO_2 (Figure 7a–c). The inflection point appeared at ~800 °C for pure CeO_2 (Figure 7a). This result suggests that CeO_2 in CeO_2/MgO was reduced faster than pure CeO_2, which is in good agreement with H_2-TPR (Figure 4).
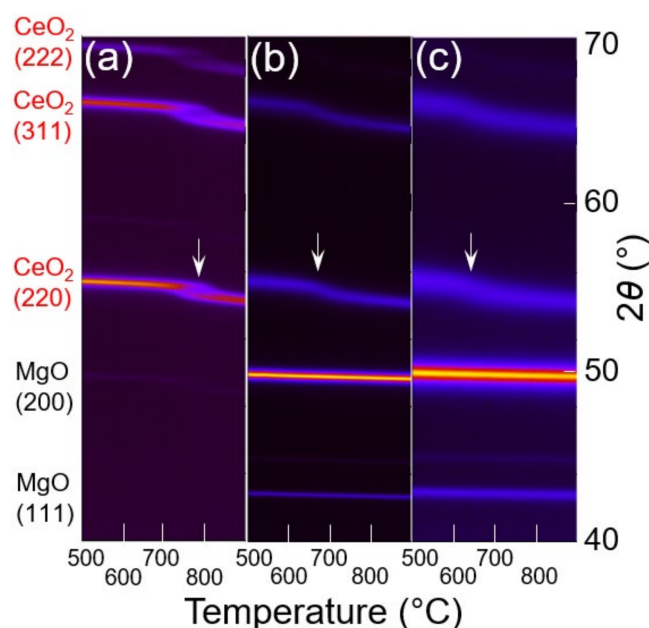
Figure 7. In situ XRD patterns of (**a**) CeO_2, (**b**) 0.05-$CeO_2/MgO(air)$, and (**c**) 0.05-$CeO_2/MgO(dry)$. A Co X-ray source and an Fe filter were used for the measurements. White arrows indicate the inflection points observed on the (220) peaks of CeO_2. The unassigned weak peaks were attributed to the diffraction of Co K-β.

Another difference between the CeO_2/MgO and the pure CeO_2 was observed in the shape of the diffraction patterns of CeO_2 (Figure 7a–c). Notably, the splitting of diffraction patterns was observed for pure CeO_2 around 2θ = ~55° and ~65° at ~750 °C (Figure 6a and Figure S4). This result suggests that the reduction proceeded heterogeneously in CeO_2 grains. As shown in Figure 4, H_2-TPR of pure CeO_2 detected a long tailing to a high temperature at >800 °C. Such tailing means that the reduction of pure CeO_2 was limited by the diffusion of oxygen in CeO_2 [61–63]. Such diffusion-controlled reduction would render the outer side of CeO_2 particles more reduced than the inner part of them. In contrast, such splitting was not observed for CeO_2/MgO catalysts. The reduction of CeO_2 nanoparticles in CeO_2/MgO proceeded more homogeneously than pure CeO_2 due to the small size of CeO_2 nanoparticles.

The variation of unit cell parameter a_0 of CeO_2 was calculated assuming that the structural change of CeO_2 nanoparticles was isotropic. The calculated values of a_0 were normalized by the values at 200 °C to see the variation depending on the temperature. As shown in Figure 8, the unit cell parameter a_0 increased at a lower temperature for 0.05-$CeO_2/MgO(dry)$ than for 0.05-$CeO_2/MgO(air)$. The first derivative of the unit cell parameter held a peak at 640 °C and 680 °C for 0.05-$CeO_2/MgO(dry)$ and 0.05-$CeO_2/MgO(air)$, respectively (Figure S5). This difference was ascribed to the smaller size of CeO_2 in 0.05-$CeO_2/MgO(dry)$. As confirmed by H_2-TPR (Figure 4), 0.05-$CeO_2/MgO(dry)$ was reduced at a lower temperature than 0.05-$CeO_2/MgO(air)$ due to the higher dispersion

of CeO_2 (Figure 3). The faster removal of the oxygen from the lattice led to the structural change at a lower temperature. In addition, structural relaxation proceeds more easily as the size of CeO_2 decreases [13,17,19]. The results of in situ XRD also demonstrated that 0.05-CeO_2/MgO(dry) was reduced at lower temperatures than 0.05-CeO_2/MgO(air).
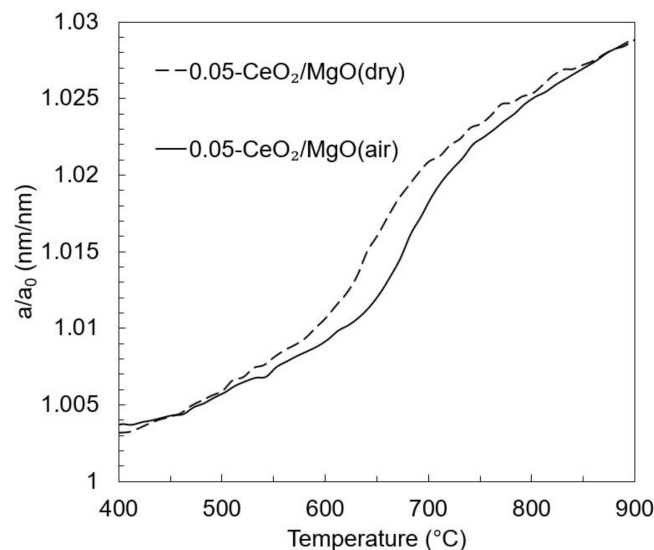
Figure 8. Unit cell parameter a_0 of CeO_2 nanoparticles of 0.05-CeO_2/MgO(air) and 0.05-CeO_2/MgO(dry) calculated from in situ XRD measurement. The vertical axis is normalized by the value of a_0 at 200 °C.

3.4. Dry Reforming Reaction

As shown in previous sections, CeO_2 nanoparticles in 0.05-CeO_2/MgO(dry) were smaller than those in 0.05-CeO_2/MgO(air). Such small CeO_2 nanoparticles led to the high mobility of the lattice oxygen. In this section, the difference of the catalysts was demonstrated via a dry reforming reaction, in which the catalysts were exposed to dry reductive gas at high temperatures. Figure 9 shows the average reaction rate of CH_4 throughout the reaction. The time course profile of the CH_4 conversion rate is also shown in Figure S6. All the catalysts remained white or yellow after the reaction, suggesting the absence of carbon deposition. Both 0.05-CeO_2/MgO(air) and 0.05-CeO_2/MgO(dry) outperformed pure CeO_2 despite their low content of CeO_2, i.e., 18.3 wt%. Further, a higher conversion was attained over 0.05-CeO_2/MgO(dry) than over 0.05-CeO_2/MgO(air). These differences were ascribed to the dispersion of CeO_2 nanoparticles. The average diameter of pure CeO_2 was 61.6 nm while those of 0.05-CeO_2/MgO(air) and 0.05-CeO_2/MgO(dry) were 6.9 nm and 4.5 nm, respectively (Table 1). The finer CeO_2 nanoparticles led to the higher surface area of CeO_2, resulting in the higher catalytic activity. In addition, 0.05-CeO_2/MgO(air) exhibited higher activity than pure CeO_2 although the area of CeO_2 in 0.05-CeO_2/MgO(air), 12.5 m^2/g, was smaller than that of pure CeO_2, 13.5 m^2/g (Table 1). Our previous study also suggests that MgO promotes CO_2 supply to the CeO_2 surface due to the strong basicity of the MgO [36]. Such interaction would also contribute to the higher catalytic activity of CeO_2/MgO.

The selectivity of the reaction is also illustrated in Figure S7 as the time course profile of the outlet gas composition. All the reaction proceeds under the reaction condition of a low conversion rate of CH_4, ~4%. Due to the low conversion rate, the selectivity of H_2 against CO was as low as 0.1–0.2 (Figure S7). Notably, the average value of H_2/CO throughout the 6-h reaction was slightly smaller for pure CeO_2, 0.11, than 0.05-CeO_2/MgO(air), 0.18, and 0.05-CeO_2/MgO(dry), 0.17. The origin of this difference is uncertain, but we attributed it to the CH_4 conversion rate and reducibility of CeO_2. As shown in Figure 9, the CH_4 conversion rate over the pure CeO_2 is lower than those over 0.05-CeO_2/MgO. This means the total supply of H_2 is less over CeO_2 than over 0.05-CeO_2/MgO, causing the difference

in the H_2/CO ratio. Another possible origin of the difference is the reducibility of CeO_2. H_2-TPR demonstrated that reduction of pure CeO_2 did not complete even at 800 °C (Figure 4). This result suggests that the pure CeO_2 continued to be reduced by the product H_2 during the reaction. Such a reaction would lead to a lower H_2/CO ratio due to the consumption of H_2.
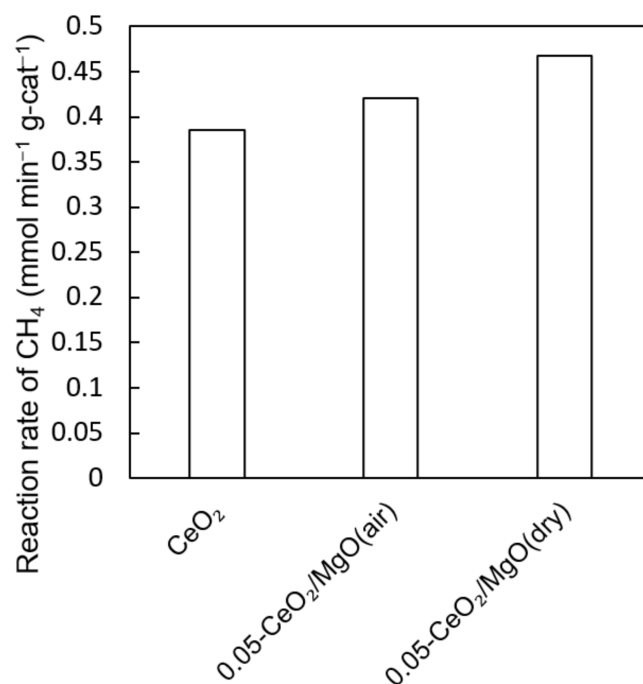

Figure 9. Average reaction rates of CH_4 of 6-h dry reforming reaction over CeO_2 and CeO_2/MgO.

The temporal variation of the CH_4 conversion rate also depended on the catalysts. The pure CeO_2 was deactivated rapidly within the initial two hours but then gradually (Figure S6). On the contrary, such an initial rapid drop of the CH_4 conversion rate was not observed for 0.05-CeO_2/MgO(air) and 0.05-CeO_2/MgO(dry). This difference in the initial behavior was attributed to the stoichiometry of the CeO_2 surface influenced by the diffusion of oxygen in the CeO_2 particles. As shown in Figure 4, the reduction of pure CeO_2 at 800 °C was diffusion controlled. The reduction did not complete even at 900 °C. This result suggests that it takes a long time to reach the equilibrium in the oxygen content of the pure CeO_2 during the reaction. Contrary, the reduction of 0.05-CeO_2/MgO(air) and 0.05-CeO_2/MgO(dry) was almost completed at 800 °C in H_2-TPR (Figure 4), suggesting that it takes a short time to reach the equilibrium in the oxygen content of CeO_2/MgO during the reaction. Therefore, there would be fewer oxygen vacancies on the surface of pure CeO_2 than on CeO_2 nanoparticles in CeO_2/MgO. Such fewer oxygen vacancies of the pure CeO_2 would improve the initial activity because previous studies reported that the C-H activation energy on CeO_2 decreased as the number of oxygen vacancies decreased [64,65].

Notably, 0.05-CeO_2/MgO(air) exhibited steady catalytic activity throughout the 6-h reaction, but 0.05-CeO_2/MgO(dry) was gradually deactivated (Figure S6). The gradual deactivation of 0.05-CeO_2/MgO(dry) was attributed to the gradual sintering of CeO_2 nanoparticles caused by the moisture content in the gas. Dry reforming produces H_2O along with H_2 and CO. Although the concentration of water in the product gas was lower than that of ambient air (Table S3), 0.05-CeO_2/MgO(dry) was exposed to the water vapor at 800 °C during the reaction, causing the structural change of 0.05-CeO_2/MgO(dry). On the contrary, 0.05-CeO_2/MgO(air) was already heated at 800 °C in the ambient air containing ~3 vol% of H_2O before the reaction (Table S3). Therefore, the byproduct H_2O in the product gas affected 0.05-CeO_2/MgO(dry) more than 0.05-CeO_2/MgO(air).

As discussed above, 0.05-CeO_2/MgO(dry) gradually deactivated during the dry reforming reaction while 0.05-CeO_2/MgO(air) exhibited stable activity. This difference in the behavior of 0.05-CeO_2/MgO(air) and 0.05-CeO_2/MgO(dry) suggests that the preparation of catalysts under the dry atmosphere is effective only for the reactions in the absence of H_2O. Solar-thermochemical reaction is an example of such reactions [7]. The solar-thermochemical reaction proceeds as a two-step reaction; the catalyst is subjected to high temperatures to be reduced thermodynamically and then re-oxidized by CO_2 at low temperatures to produce CO. The CeO_2/MgO(dry) would be suitable for the reaction since it demonstrated high stability and reducibility under dry conditions (Figures 4 and 5).

4. Conclusions

This study demonstrated that stable CeO_2 nanoparticles were deposited on MgO by the simple impregnation method. When CeO_2/MgO was prepared under the dry atmosphere, the CeO_2 nanoparticles remained ~3 nm in diameter even after being heated at 800 °C, which is much smaller than ~5 nm of CeO_2/MgO prepared under ambient air. The difference was attributed to the higher surface area of the catalysts prepared under the dry atmosphere. H_2-TPR, CO_2-TPO, XPS, and in situ XRD showed that CeO_2/MgO(dry) exhibited higher oxygen mobility than CeO_2/MgO(air) due to the higher dispersion of CeO_2 nanoparticles. The higher catalytic activity of CeO_2/MgO(dry) than CeO_2/MgO(air) was also demonstrated by the dry reforming reaction.

References

1. Trovarelli, A. Catalytic properties of ceria and CeO_2-Containing materials. *Catal. Rev.-Sci. Eng.* **1996**, *38*, 439–520. [CrossRef]
2. Yang, X.; Da, J.; Yu, H.; Wang, H. Characterization and performance evaluation of Ni-based catalysts with Ce promoter for methane and hydrocarbons steam reforming process. *Fuel* **2016**, *179*, 353–361. [CrossRef]
3. Savuto, E.; Navarro, R.M.; Mota, N.; Di Carlo, A.; Bocci, E.; Carlini, M.; Fierro, J.L.G. Steam reforming of tar model compounds over Ni/Mayenite catalysts: Effect of Ce addition. *Fuel* **2018**, *224*, 676–686. [CrossRef]
4. Gac, W.; Zawadzki, W.; Rotko, M.; Słowik, G.; Greluk, M. CO_2 Methanation in the Presence of Ce-Promoted Alumina Supported Nickel Catalysts: H_2S Deactivation Studies. *Top. Catal.* **2019**, *62*, 524–534. [CrossRef]
5. Yeo, T.Y.; Ashok, J.; Kawi, S. Recent developments in sulphur-resilient catalytic systems for syngas production. *Renew. Sustain. Energy Rev.* **2019**, *100*, 52–70. [CrossRef]
6. Nair, M.M.; Abanades, S. Tailoring Hybrid Nonstoichiometric Ceria Redox Cycle for Combined Solar Methane Reforming and Thermochemical Conversion of H_2O/CO_2. *Energy Fuels* **2016**, *30*, 6050–6058. [CrossRef]

7. Arifin, D.; Weimer, A.W. Kinetics and mechanism of solar-thermochemical H_2 and CO production by oxidation of reduced CeO_2. *Sol. Energy* **2018**, *160*, 178–185. [CrossRef]

8. Zheng, Y.; Li, K.; Wang, H.; Tian, D.; Wang, Y.; Zhu, X.; Wei, Y.; Zheng, M.; Luo, Y. Designed oxygen carriers from macroporous $LaFeO_3$ supported CeO_2 for chemical-looping reforming of methane. *Appl. Catal. B Environ.* **2017**, *202*, 51–63. [CrossRef]

9. Galvita, V.V.; Poelman, H.; Bliznuk, V.; Detavernier, C.; Marin, G.B. CeO_2-Modified Fe_2O_3 for CO_2 Utilization via Chemical Looping. *Ind. Eng. Chem. Res.* **2013**, *52*, 8416–8426. [CrossRef]

10. Zaimes, G.G.; Hubler, B.J.; Wang, S.; Khanna, V. Environmental life cycle perspective on rare earth oxide production. *ACS Sustain. Chem. Eng.* **2015**, *3*, 237–244. [CrossRef]

11. Haque, N.; Hughes, A.; Lim, S.; Vernon, C. Rare earth elements: Overview of mining, mineralogy, uses, sustainability and environmental impact. *Resources* **2014**, *3*, 614–635. [CrossRef]

12. Lin, Y.; Wu, Z.; Wen, J.; Poeppelmeier, K.R.; Marks, L.D. Imaging the atomic surface structures of CeO_2 nanoparticles. *Nano Lett.* **2014**, *14*, 191–196. [CrossRef]

13. Paun, C.; Safonova, O.V.; Szlachetko, J.; Abdala, P.M.; Nachtegaal, M.; Sa, J.; Kleymenov, E.; Cervellino, A.; Krumeich, F.; Van Bokhoven, J.A. Polyhedral CeO_2 nanoparticles: Size-dependent geometrical and electronic structure. *J. Phys. Chem. C* **2012**, *116*, 7312–7317. [CrossRef]

14. Matei-Rutkovska, F.; Postole, G.; Rotaru, C.G.; Florea, M.; Pârvulescu, V.I.; Gelin, P. Synthesis of ceria nanopowders by microwave-assisted hydrothermal method for dry reforming of methane. *Int. J. Hydrog. Energy* **2016**, *41*, 2512–2525. [CrossRef]

15. Laosiripojana, N.; Charojrochkul, S.; Kim-lohsoontorn, P.; Assabumrungrat, S. Role and advantages of H_2S in catalytic steam reforming over nanoscale CeO_2 -based catalysts. *J. Catal.* **2010**, *276*, 6–15. [CrossRef]

16. Wu, Z.; Zhang, J.; Benfield, R.E.; Ding, Y.; Grandjean, D.; Zhang, Z.; Ju, X. Structure and Chemical Transformation in Cerium Oxide Nanoparticles Coated by Surfactant Cetyltrimethylammonium Bromide (CTAB): An X-ray Absorption Spectroscopic Study. *J. Phys. Chem. B* **2002**, *106*, 4569–4577. [CrossRef]

17. Zhang, F.; Chan, S.W.; Spanier, J.E.; Apak, E.; Jin, Q.; Robinson, R.D.; Herman, I.P. Cerium oxide nanoparticles: Size-selective formation and structure analysis. *Appl. Phys. Lett.* **2002**, *80*, 127–129. [CrossRef]

18. Natile, M.M.; Boccaletti, G.; Glisenti, A. Properties and reactivity of nanostructured CeO_2 powders: Comparison among two synthesis procedures. *Chem. Mater.* **2005**, *17*, 6272–6286. [CrossRef]

19. Spanier, J.E.; Robinson, R.D.; Zhang, F.; Chan, S.; Herman, I.P. Size-dependent properties of CeO_{2-y} nanoparticles as studied by Raman scattering. *Phys. Rev. B* **2001**, *64*, 245407. [CrossRef]

20. Hailstone, R.K.; DiFrancesco, A.G.; Leong, J.G.; Allston, T.D.; Reed, K.J. A study of lattice expansion in CeO_2 Nanoparticles by Transmission Electron Microscopy. *J. Phys. Chem. C* **2009**, *113*, 15155–15159. [CrossRef]

21. Han, W.Q.; Wen, W.; Hanson, J.C.; Teng, X.; Marinkovic, N.; Rodriguez, J.A. One-dimensional ceria as catalyst for the low-temperature water-gas shift reaction. *J. Phys. Chem. C* **2009**, *113*, 21949–21955. [CrossRef]

22. Zhang, J.; Kumagai, H.; Yamamura, K.; Ohara, S.; Takami, S.; Morikawa, A.; Shinjoh, H.; Kaneko, K.; Adschiri, T.; Suda, A. Extra-Low-Temperature Oxygen Storage Capacity of CeO_2 Nanocrystals with Cubic Facets. *Nano Lett.* **2011**, *11*, 361–364. [CrossRef] [PubMed]

23. Aneggi, E.; Wiater, D.; de Leitenburg, C.; Llorca, J.; Trovarelli, A. Shape-Dependent Activity of Ceria in Soot Combustion. *ACS Catal.* **2014**, *4*, 172–181. [CrossRef]

24. Liu, Z.; Sorrell, C.C.; Koshy, P.; Hart, J.N. DFT Study of Methanol Adsorption on Defect-Free CeO_2 Low-Index Surfaces. *ChemPhysChem* **2019**, *20*, 2074–2081. [CrossRef]

25. Branda, M.M.; Ferullo, R.M.; Causá, M.; Illas, F. Relative stabilities of low index and stepped CeO_2 surfaces from hybrid and GGA + U implementations of density functional theory. *J. Phys. Chem. C* **2011**, *115*, 3716–3721. [CrossRef]

26. Damyanova, S.; Bueno, J.M.C. Effect of CeO_2 loading on the surface and catalytic behaviors of CeO_2-Al_2O_3-supported Pt catalysts. *Appl. Catal. A Gen.* **2003**, *253*, 135–150. [CrossRef]

27. Reddy, B.M.; Rao, K.N.; Reddy, G.K.; Khan, A.; Park, S.E. Structural characterization and oxidehydrogenation activity of CeO 2/Al2O3 and V2O5/ CeO2ZAl2O3 catalysts. *J. Phys. Chem. C* **2007**, *111*, 18751–18758. [CrossRef]

28. Shyu, J.Z.; Weber, W.H.; Gandhi, H.S. Surface characterization of alumina-supported ceria. *J. Phys. Chem.* **1988**, *92*, 4964–4970. [CrossRef]

29. Beniya, A.; Isomura, N.; Hirata, H.; Watanabe, Y. Morphology and chemical states of size-selected Pt n clusters on an aluminium oxide film on NiAl(110). *Phys. Chem. Chem. Phys.* **2014**, *16*, 26485–26492. [CrossRef] [PubMed]

30. Ma, Y.; Ma, Y.; Li, J.; Li, Q.; Hu, X.; Ye, Z.; Wu, X.Y.; Buckley, C.E.; Dong, D. CeO_2-promotion of $NiAl_2O_4$ reduction via $CeAlO_3$ formation for efficient methane reforming. *J. Energy Inst.* **2020**, *93*, 991–999. [CrossRef]

31. Nataliya Bochvar, N.; Liberov, Y.; Fabrichnaya, O.; MSIT®. Ce-Mg-O Ternary Phase Diagram Evaluation. Available online: https://materials.springer.com/msi/docs/sm_msi_r_10_012253_02 (accessed on 26 November 2020).

32. Tinoco, M.; Sanchez, J.J.; Yeste, M.P.; Lopez-Haro, M.; Trasobares, S.; Hungria, A.B.; Bayle-guillemaud, P.; Blanco, G.; Pintado, J.M.; Calvino, J.J. Low-Lanthanide-Content CeO_2/MgO Catalysts with Outstandingly Stable Oxygen Storage Capacities: An In-Depth Structural Characterization by Advanced STEM Techniques. *ChemCatChem* **2015**, *7*, 3763–3778. [CrossRef]

33. Pérez Casero, R.; Gómez San Román, R.; Perrière, J.; Laurent, A.; Seiler, W.; Gergaud, P.; Keller, D. Epitaxial growth of CeO_2 on MgO by pulsed laser deposition. *Appl. Surf. Sci.* **1997**, *109–110*, 341–344. [CrossRef]

34. Paunović, V.; Zichittella, G.; Mitchell, S.; Hauert, R.; Pérez-Ramírez, J. Selective Methane Oxybromination over Nanostructured Ceria Catalysts. *ACS Catal.* **2018**, *8*, 291–303. [CrossRef]

35. Plewa, J.; Steindor, J. Kinetics of reduction of magnesium sulfate by carbon oxide. *J. Therm. Anal.* **1987**, *32*, 1809–1820. [CrossRef]

36. Taira, K. Dry reforming reactions of CH4 over CeO2/MgO catalysts at high concentrations of H2S. 2021, J. Cat. Under revision. *J. Cat.* Under revision.. **2021**.

37. Ferreira, V.J.; Tavares, P.; Figueiredo, J.L.; Faria, J.L. Effect of Mg, Ca, and Sr on CeO$_2$ based catalysts for the oxidative coupling of methane: Investigation on the oxygen species responsible for catalytic performance. *Ind. Eng. Chem. Res.* **2012**, *51*, 10535–10541. [CrossRef]

38. Geysermans, P.; Finocchi, F.; Goniakowski, J.; Hacquart, R.; Jupille, J. Combination of (100), (110) and (111) facets in MgO crystals shapes from dry to wet environment. *Phys. Chem. Chem. Phys.* **2009**, *11*, 2228–2233. [CrossRef] [PubMed]

39. Holt, S.A.; Jones, C.F.; Watson, G.S.; Crossley, A.; Johnston, C. Surface modification of MgO substrates from aqueous exposure: An atomic force microscopy study. *Thin Solid Film.* **1997**, *292*, 96–102. [CrossRef]

40. Eastman, P.F.; Culter, I.B. Effect of Water Vapor on Initial Sintering of Magnesia. *J. Am. Ceram. Soc.* **1966**, *49*, 526–530. [CrossRef]

41. Ito, T.; Fujita, M.; Watanabe, M.; Tokuda, T. The initial sintering of alkaline earth oxides in water vapor and hydrogen gas. *Bull. Cemical Soc. Japan* **1981**, *54*, 2412–2419. [CrossRef]

42. Green, J. Calcination of precipitated Mg(OH)$_2$ to active MgO in the production of refractory and chemical grade MgO. *J. Mater. Sci.* **1983**, *18*, 637–651. [CrossRef]

43. Peng, C.; Zhang, Z. Nitrate–citrate combustion synthesis of Ce$_{1-x}$Gd$_x$O$_{2-x/2}$ powder and its characterization. *Ceram. Int.* **2007**, *33*, 1133–1136. [CrossRef]

44. Taira, K.; Nakao, K.; Suzuki, K.; Einaga, H. SO$_x$ tolerant Pt/TiO$_2$ catalysts for CO oxidation and the effect of TiO$_2$ supports on catalytic activity. *Environ. Sci. Technol.* **2016**, *50*, 9773–9780. [CrossRef] [PubMed]

45. Burroughs, P.; Hamnett, A.; Orchard, A.F.; Thornton, G. Satellite structure in the X-ray photoelectron spectra of some binary and mixed oxides of lanthanum and cerium. *J. Chem. Soc. Dalt. Trans.* **1976**, 1686. [CrossRef]

46. Romeo, M.; Bak, K.; El Fallah, J.; Le Normand, F.; Hilaire, L. XPS Study of the reduction of cerium dioxide. *Surf. Interface Anal.* **1993**, *20*, 508–512. [CrossRef]

47. National Institute of Standards and Technology. *NIST X-Ray Photoelectron Spectroscopy Database*; NIST Standard Reference Database Number 20; National Institute of Standards and Technology: Gaithersburg, MD, USA, 2000. [CrossRef]

48. Della Mea, G.B.; Matte, L.P.; Thill, A.S.; Lobato, F.O.; Benvenutti, E.V.; Arenas, L.T.; Jürgensen, A.; Hergenröder, R.; Poletto, F.; Bernardi, F. Tuning the oxygen vacancy population of cerium oxide (CeO$_{2-x}$, 0 <x <0.5) nanoparticles. *Appl. Surf. Sci.* **2017**, *422*, 1102–1112. [CrossRef]

49. Taira, K.; Sugiyama, T.; Einaga, H.; Nakao, K.; Suzuki, K. Promoting effect of 2000 ppm H$_2$S on the dry reforming reaction of CH$_4$ over pure CeO$_2$, and in situ observation of the behavior of sulfur during the reaction. *J. Catal.* **2020**, *389*, 611–622. [CrossRef]

50. Beruto, D.; Botter, R.; Searcy, A.W. H$_2$O-Catalyzed Sintering of ~2-nm-Cross-Section Particles of MgO. *J. Am. Ceram. Soc.* **1987**, *70*, 155–159. [CrossRef]

51. Cadigan, C.A.; Corpuz, A.R.; Lin, F.; Caskey, C.M.; Finch, K.B.H.; Wang, X.; Richards, R.M. Nanoscale (111) faceted rock-salt metal oxides in catalysis. *Catal. Sci. Technol.* **2013**, *3*, 900–911. [CrossRef]

52. Gottlieb, H.E.; Kotlyar, V.; Nudelman, A. NMR chemical shifts of common laboratory solvents as trace impurities. *J. Org. Chem.* **1997**, *3263*, 7512–7515. [CrossRef] [PubMed]

53. Sangwal, K. Mechanism of dissolution of MgO crystals in acids. *J. Mater. Sci.* **1980**, *15*, 237–246. [CrossRef]

54. Filley, J.; Ibrahim, M.A.; Nimlos, M.R.; Watt, A.S.; Blake, D.M. Magnesium and calcium chelation by a bis-spiropyran. *J. Photochem. Photobiol. A Chem.* **1998**, *117*, 193–198. [CrossRef]

55. Hu, Y.; Lee, B.; Bell, C.; Jun, Y.-S. Environmentally Abundant Anions Influence the Nucleation, Growth, Ostwald Ripening, and Aggregation of Hydrous Fe(III) Oxides. *Langmuir* **2012**, *28*, 7737–7746. [CrossRef]

56. Karen, P.; Kjekshus, A.; Huang, Q.; Karen, V.L. The crystal structure of magnesium dicarbide. *J. Alloys Compd.* **1999**, *282*, 72–75. [CrossRef]

57. McBride, J.R.; Hass, K.C.; Poindexter, B.D.; Weber, W.H. Raman and X-ray studies of Ce$_{1-x}$RE$_x$O$_{2-y}$, where RE=La, Pr, Nd, Eu, Gd, and Tb. *J. Appl. Phys.* **1994**, *76*, 2435–2441. [CrossRef]

58. Holgado, J.P.; Alvarez, R.; Munuera, G. Study of CeO$_2$ XPS spectra by factor analysis: Reduction of CeO$_2$. *Appl. Surf. Sci.* **2000**, *161*, 301–315. [CrossRef]

59. Galvita, V.V.; Poelman, H.; Rampelberg, G.; De Schutter, B.; Detavernier, C.; Marin, G.B. Structural and kinetic study of the reduction of CuO-CeO$_2$/Al$_2$O$_3$ by time-resolved X-ray diffraction. *Catal. Lett.* **2012**, *142*, 959–968. [CrossRef]

60. Perrichon, V.; Laachir, A.; Bergeret, G.; Fréty, R.; Tournayan, L.; Touret, O. Reduction of cerias with different textures by hydrogen and their reoxidation by oxygen. *J. Chem. Soc. Faraday Trans.* **1994**, *90*, 773–781. [CrossRef]

61. Stan, M.; Zhu, Y.T.; Jiang, H.; Butt, D.P. Kinetics of oxygen removal from ceria. *J. Appl. Phys.* **2004**, *95*, 3358–3361. [CrossRef]

62. Al-Madfaa, H.A.; Khader, M.M. Reduction kinetics of ceria surface by hydrogen. *Mater. Chem. Phys.* **2004**, *86*, 180–188. [CrossRef]

63. Goguet, A.; Meunier, F.C.; Tibiletti, D.; Breen, J.P.; Burch, R. Spectrokinetic Investigation of Reverse Water-Gas-Shift Reaction Intermediates over a Pt/CeO$_2$ Catalyst. *J. Phys. Chem. B* **2004**, *108*, 20240–20246. [CrossRef]

64. Warren, K.J.; Scheffe, J.R. Role of Surface Oxygen Vacancy Concentration on the Dissociation of Methane over Nonstoichiometric Ceria. *J. Phys. Chem. C* **2019**, *123*, 13208–13218. [CrossRef]
65. Kumar, G.; Lau, S.L.J.; Krcha, M.D.; Janik, M.J. Correlation of Methane Activation and Oxide Catalyst Reducibility and Its Implications for Oxidative Coupling. *ACS Catal.* **2016**, *6*, 1812–1821. [CrossRef]